Research Article | Open Access

Soft Science

Qiao et al. Soft Sci. 2026, 6, 96 DOI:10.20517/ss.2026.173

Thermally switchable gauge-factor bits for multilevel gain coding in reversible shape-memory strain sensor arrays

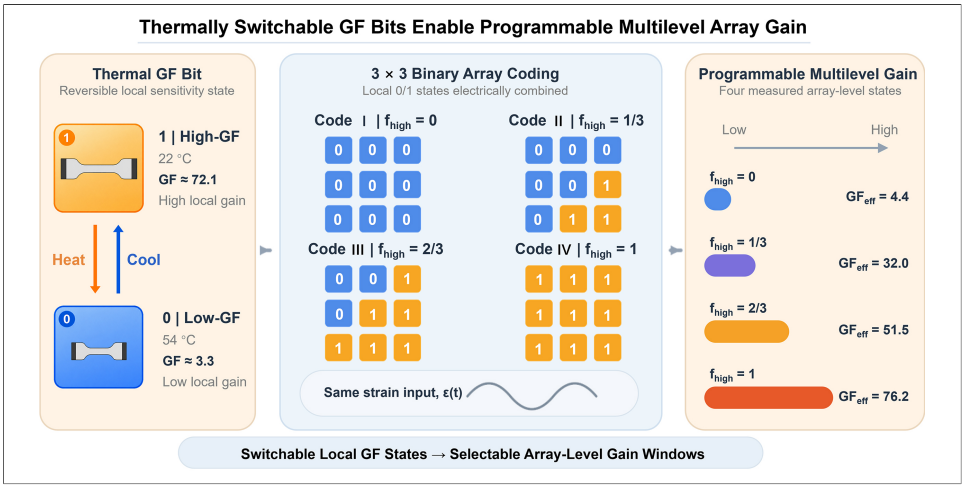
Wenjie Qiao#, Zichao Wang#, Lehua Dong, Hanyu Cui, Ting Wang, Xuefeng Zhu, Chao Yang, Yuehan Wang, Xuan Zhang*, Jie Kong*

Keywords:
Gauge-factor bit, flexible strain sensor, reversible shape-memory polymer, programmable gain, effective gauge factor, multilevel gain coding, sensing-window matching

Citation: Qiao, W.; Wang, Z.; Dong, L.; Cui, H.; Wang, T.; Zhu, X.; Yang, C.; Wang, Y.; Zhang, X.; Kong, J. Thermally switchable gauge-factor bits for multilevel gain coding in reversible shape-memory strain sensor arrays. *Soft Sci.* **2026**, *6*, 96. https://dx.doi.org/10.20517/ss.2026.173

Received: 30 Jun 2026
First Decision: 29 Jul 2026
Revised: 26 Aug 2026
Accepted: 31 Aug 2026
Published: 15 Oct 2026

Academic Editors: YongAn Huang, Wei Gao
Copy Editor: Pei-Yun Wang
Production Editor: Pei-Yun Wang



Abstract

Flexible strain sensors are typically constructed with a fixed gauge factor (GF), making it difficult for sensor arrays to accommodate weak, moderate, and strong mechanical inputs within a single system. Here, we report a thermally switchable GF-bit strain-sensing system based on a reversible shape-memory polymer/carbon black composite. Thermal stimulation reversibly changes the programmed polymer shape state and the strain-dependent response of the conductive network, whereas mechanical strain serves as the sensing readout input. A single sensing pixel switches between a heated low-GF state and a room-temperature high-GF state, with GF values of 3.3 and 72.1, respectively, corresponding to an approximately 22-fold difference. The two GF states remained distinguishable over 50 thermal switching cycles, and a representative single-sensor erase-and-reprogram test yielded low- and high-GF values close to their corresponding initial values. Temperature-dependent measurements identified a high-GF regime over the tested range of 5-45 °C, a pronounced transition toward the low-GF state over approximately 45-54 °C, and a low-GF plateau over the tested range of 54-70 °C. By integrating GF bits

MOE Key Lab of Materials Physics and Chemistry in Extraordinary Conditions, Shaanxi Key Lab of Macromolecular Science and Technology, School of Chemistry and Chemical Engineering, Northwestern Polytechnical University, Xi'an 710072, Shaanxi, China.
#These authors contributed equally to this work.

***Correspondence to:** Assoc. Prof. Xuan Zhang, Prof. Jie Kong, Shaanxi Key Lab of Macromolecular Science and Technology, School of Chemistry and Chemical Engineering, Northwestern Polytechnical University, Xi'an 710072, Shaanxi, China. E-mail: zhangxuan@nwpu.edu.cn; kongjie@nwpu.edu.cn

into series, parallel, and 3 × 3 electrical arrays, local binary states were converted into discrete array-level effective-GF outputs that were quantitatively described using a finite-strain circuit model based on exact series/parallel circuit relations. The resulting high-, intermediate-, and low-effective-GF states provide different output windows under the same nominal mechanical-input protocol. These results demonstrate that GF can be converted from a fixed post-fabrication parameter into a thermally switchable and electrically combinable gain state for programmable flexible sensor arrays.

INTRODUCTION

Flexible strain sensors convert mechanical deformation into electrical signals and are widely used in wearable electronics, soft robotics, human–machine interfaces, and health-monitoring systems[1-6]. Their sensitivity is commonly described by the gauge factor (GF), which is defined as the relative resistance change per unit strain[7-9]. However, the GF remains a fixed scalar parameter set during fabrication by the material composition, conductive-network morphology, and device architecture in most flexible strain sensors[7-12]. Moreover, sensors with high sensitivity, a wide detection range, or good cycling stability usually retain one fixed gain state after fabrication[9-12]. Flexible sensing systems are evolving from single-point readout systems toward arrayed, multifunctional, and wide-dynamic-range monitoring[13-15]. In these settings, a fixed GF limits the ability of a sensor to match different signal windows[16]. This limitation is particularly important in distributed sensor arrays, where different pixels may experience local mechanical inputs with substantially different amplitudes[14,15]. Therefore, programmable local gain matching is needed to prevent weak signals from being lost and strong signals from being excessively amplified[11,16]. Simply maximizing GF does not address this requirement, because weak, moderate, and strong mechanical-input regimes can benefit from different sensing gains. This consideration motivates the conversion of GF from a fixed post-fabrication parameter into a switchable, discretizable, and electrically combinable gain state for array-level multilevel gain coding.

To extend beyond programmable sensitivity regulation[16-18], the GF state of a single sensing pixel can be further defined as a discrete 0/1 GF bit. Here, a GF bit refers to a local gain unit whose GF can be switched between two distinguishable and repeatable states, and it does not refer to a one-time GF change. Instead, it represents a local sensitivity state that can be thermally switched and then combined with other pixels, in which reversible shape-state regulation serves as the material basis[19-23]. Multiple GF bits can then be electrically integrated into arrays to convert local binary GF states into an array-level effective GF output[24-26]. In this system, the GF is no longer only a performance metric of a single device, and it can be extended to a programmable system-level gain parameter at the array scale, reflecting the function of structure–performance-programmable materials[27]. The key feature of a GF bit is therefore not the magnitude of a single GF value, but the ability to discretize sensitivity into repeatably switchable 0/1 units and combine them into low, intermediate, and high effective GF outputs.

Existing sensitivity-regulation strategies have mainly focused on increasing, broadening, or tuning the GF, rather than discretizing the GF into switchable 0/1 states for array-level gain coding[9,18,28,29]. Conductive-filler loading, percolation-network optimization, microstructural design, and encapsulation strategies can be used to improve the GF or broaden the sensing range[7,8,30-32]. In these approaches, the sensing characteristics are usually set during fabrication and are difficult to alter during operation. Crack engineering, near-percolation conductive networks, and strain-concentrating structures can amplify resistance changes and yield high sensitivity[11,17,33,34]. However, these high-gain mechanisms often rely on fragile conductive contacts or controlled crack evolution, which can lead to contact drift, irreversible structural changes, or cycling instability. Such features make these mechanisms difficult to use as repeatably switchable local 0/1 gain units. While mechanical presetting, 4D-printed shape-changing materials, and shape-memory-assisted sensors can

also change sensitivity through structural reconfiguration, most of these strategies remain focused on single-device sensitivity modulation or require external mechanical programming to change the device state[18,35-37]. Although previous studies have enabled the enhancement, broadening, or post-fabrication regulation of GF, most have focused on changing the sensitivity of individual devices rather than defining electrically combinable local gain states. To the best of our knowledge, a GF-bit scheme that integrates reversible local GF switching, deliberate discretization into binary gain states, and array-level electrical gain coding remains largely unexplored. To clarify this distinction, representative fixed-GF, post-tunable, mechanically programmed, and shape-reconfigurable sensing strategies are compared with the GF-bit approach developed in this study [Supplementary Table 1]. The present system combines thermally addressable local GF switching, discrete 0/1 gain states, and electrical integration of these local states into multilevel effective-GF outputs.

Variation of the GF value alone is insufficient when applying a thermally switchable GF bit in array-level gain coding. Such a bit must also provide distinguishable local GF states, reversible switching without repeated mechanical reprogramming, and conversion into a multilevel effective GF through array coding. A large GF contrast usually requires a marked change in the electrical transport state of the conductive network. Many high-sensitivity networks achieve such a contrast through near-percolation contacts, crack amplification, or microstructural deformation; however, these mechanisms can introduce irreversible evolution, baseline drift, or cycling instability[11,17,33,38]. Switching during use also requires conductive-network modulation without repeated prestretching, compression, or mechanically imposed reconstruction. This remains difficult for many mechanically programmed sensitivity-tuning strategies[16,18,37]. In addition, array coding requires the integration of high- and low-GF units in one electrical array, which must produce distinguishable multilevel effective GF outputs through binary coding rules[14,24-26]. Strategies that combine reversible thermal switching, operation without repeated mechanical reprogramming, and array-level gain coding remain underdeveloped. Therefore, a material design strategy is needed in which a reversible shape state, as demonstrated in recent shape-memory polymer systems, can be repeatedly coupled to changes in the electrical response of a conductive network and further mapped into a 0/1 GF state[19,20,22,23,39].

Here, we report a thermally switchable and array-encoded GF-bit strain-sensing system based on a reversible shape-memory polymer (rSMP)/carbon black (CB) composite network. In this system, thermal shape-state switching changes the electrical response of the CB network, likely through changes in conductive contacts, filler-network configuration, and transport pathways[22,23,35]. This process is distinct from a simple thermoresistive response, as thermal stimulation serves as the input for GF-state switching, whereas mechanical strain serves as the sensing readout input. After thermally induced shape reconstruction, the resistance-response slope under the same mechanical readout strain is reversibly switched, thereby mapping the programmed shape state into a GF state. At the single-pixel level, the composite network switches between a room-temperature, high-GF state and a heated, low-GF state with an approximately 22-fold initial GF contrast. The two gain states remain well separated over the initial 20 thermal switching cycles and remain distinguishable during extended testing to 50 cycles. Moreover, in a representative recovery test conducted after cycling-induced attenuation, high-temperature erasing followed by thermomechanical reprogramming restored the low- and high-GF states to values close to their initial levels, demonstrating recoverability of the programmed GF-bit state under the tested recovery protocol. At the array level, high- and low-GF units are integrated into 1 × 2, 2 × 1, 1 × 3, 3 × 1, and 3 × 3 electrical arrays, converting binary switching into multilevel effective GF outputs. Finally, we use the GF-bit arrays to demonstrate sensing-window matching under simulated photothermal/thermal elevation conditions, including contact-induced outputs and deformation readout. Together, these results connect reversible shape-memory deformation, conductive-network modulation, local GF-bit switching, and array-level effective GF coding, providing a material-state-based strategy for programmable-gain flexible sensor arrays.

EXPERIMENTAL

Materials

1,4-Bis-[4-(6-acryloyloxyhexyloxy)benzoyloxy]-2-methylbenzene (RM82) was purchased from Sigma-Aldrich (Shanghai) Co., Ltd. Triethylamine, diethylene glycol, methanol, diphenyl(2,4,6-trimethylbenzoyl)phosphine oxide (TPO), dichloromethane (DCM), and pentaerythritol tetrakis(3-mercaptopropionate) (PTME) were purchased from Shanghai Aladdin Biochemical Technology Co., Ltd. Dibutyltin oxide (DBTO) and pentadecanolide were purchased from Shanghai Macklin Biochemical Technology Co., Ltd. Acryloyl chloride, petroleum ether, poly(ethylene glycol) diacrylate (PEGDA, M_n = 200), 1,2-bis(2-mercaptoethoxy)ethane (EDDT), and butylated hydroxytoluene (BHT) were purchased from Shanghai Titan Scientific Co., Ltd. Toluene was purchased from China National Pharmaceutical Group Co., Ltd. CB (average particle diameter ≈ 15 nm) was purchased from Cabot Corporation, and CF-10 was purchased from Dow Chemical Company. All chemicals were used as received unless otherwise specified. The deuterated chloroform ($CDCl_3$) used for ^{1}H nuclear magnetic resonance (NMR) measurements was purchased from Shanghai Aladdin Biochemical Technology Co., Ltd. 3M 1181 double-sided conductive copper foil tape was purchased from 3M Company (USA). A two-component liquid silicone (components 404A and 404B; mixing ratio A:B = 1:1 by mass) was purchased from Dongguan Xinbang New Material Co., Ltd.

Characterization and measurements

^{1}H NMR spectra were recorded using a Bruker Avance 400 MHz NMR spectrometer (Bruker, Germany) with $CDCl_3$ as the solvent. Differential scanning calorimetry (DSC) was performed using a DSC 3 differential scanning calorimeter (Mettler-Toledo, Switzerland) under a nitrogen atmosphere. The samples were subjected to heating and cooling scans over a temperature range of 10-110 °C at a rate of 2 °C·min^{-1}.

Electromechanical measurements were performed using a CMT-20 electronic universal testing machine (Jinan Lianggong Testing Technology Co., Ltd., China) combined with a Keithley 2450 SourceMeter (Keithley Instruments, USA). Mechanical strain was applied at a tensile rate of 2 mm·min^{-1} with an initial gauge length of 12 mm, while the electrical resistance was simultaneously recorded using a two-probe configuration.

Temperature-dependent sensing measurements were conducted using an LXZ-1015 temperature-controlled stage (Shenzhen Luxianzi Technology Co., Ltd., China). The surface temperature of the sensor was monitored using a DLX-HC2508 infrared (IR) thermometer (Delixi Electric Co., Ltd., China). Photothermal heating was provided by a 250 W broadband IR light source with a spectral range of 0.76-5 μm [Philips Electronics (China) Group, China].

UV photopolymerization was performed using a 365 nm UV lamp (Zhongshan Xingxuzi Lighting Co., Ltd., China) at an irradiation intensity of 20 mW·cm^{-2}. Ultrasonic dispersion was carried out using an F-020SD ultrasonic system (Shenzhen Fuyang Technology Group Co., Ltd., China). Oscillatory rheological measurements were performed using a DHR-20 rotational rheometer (TA Instruments, USA).

Oscillatory temperature-sweep rheological measurements were performed using a DHR-20 rotational rheometer (TA Instruments, USA) equipped with a 25-mm parallel-plate geometry. Measurements were conducted at a strain amplitude of 0.1%, an angular frequency of 10 rad·s^{-1}, and a gap of 0.2 mm. The temperature was increased from approximately 30 to 110 °C at a rate of 2 °C·min^{-1}, while the storage modulus (G′) and loss modulus (G″) were continuously recorded. Separate rSMP/CB specimens were subjected to 0, 20, or 50 prior GF-switching cycles between 22 and 54 °C before rheological characterization.

One heating temperature sweep was subsequently performed for each preconditioned specimen under identical conditions.

Preparation of CB/CF-10 composites

CB and CF-10 were combined at a mass ratio of 1:1.5. CF-10 was first dispersed in toluene (2 mL) and ultrasonicated using an F-020SD ultrasonic system (Shenzhen Fuyang Technology Group Co., Ltd., China) for 10 min. The resulting dispersion was then transferred into an agate mortar containing the corresponding amount of CB and manually ground for 10 min until a homogeneous CB/CF-10 composite was obtained.

Preparation of polypentadecanolide

Poly(pentadecanolide) (PPDL) was synthesized by bulk ring-opening polymerization of pentadecanolide using diethylene glycol as the initiator and DBTO as the catalyst. Briefly, pentadecanolide (20 g), diethylene glycol (0.21 g), and DBTO (0.20 g) were added to a 100 mL round-bottom flask. The reaction mixture was mechanically stirred at 500 rpm at 130 °C for 10 h under a nitrogen atmosphere. After the reaction, the crude product was dissolved in toluene to remove unreacted monomer and low-molecular-weight byproducts. The toluene solution was then slowly poured into excess methanol to induce precipitation. The precipitation process was repeated twice to further purify the polymer. The precipitate was collected and dried under a vacuum at 50 °C for 24 h to remove residual solvent, yielding the final PPDL product. The chemical structure of PPDL was confirmed by ^{1}H NMR spectroscopy [Supplementary Figure 1].

Preparation of poly(pentadecanolide) diacrylate

PPDL was end-functionalized with acryloyl chloride to obtain poly(pentadecanolide) diacrylate (PPDL-DA). PPDL (20 g) was dissolved in toluene (100 g) in a 250 mL three-neck round-bottom flask equipped with a dropping funnel under nitrogen. The solution was heated to 80 °C until complete dissolution. Triethylamine was then added as an acid scavenger at 5 molar equivalents relative to the hydroxyl groups of PPDL. Acryloyl chloride, diluted in anhydrous DCM, was added dropwise at 10 molar equivalents relative to the hydroxyl groups of PPDL. The reaction mixture was stirred at 500 rpm at 80 °C for 20 h under a nitrogen atmosphere. After the reaction, the triethylamine hydrochloride salt was removed by vacuum filtration. The filtrate was precipitated in ice-cold petroleum ether and collected by centrifugation. The product was redissolved in a small amount of DCM and reprecipitated in petroleum ether for further purification. The purified product was then dried under a vacuum at 50 °C for 24 h to obtain PPDL-DA as a white semicrystalline solid. The chemical structure of PPDL-DA was confirmed by ^{1}H NMR spectroscopy [Supplementary Figure 2].

Synthesis of the liquid-crystalline oligomer

The liquid-crystalline oligomer (LCO) was synthesized through a thiol–acrylate Michael addition reaction using RM82 and PEGDA as acrylate monomers and EDDT as a dithiol chain extender. RM82 (10.00 g) and PEGDA (1.276 g) were dissolved in toluene (10 g) in a 50 mL round-bottom flask. EDDT (1.935 g) was then added, followed by triethylamine (2 wt% relative to the total monomer mass) as the catalyst and BHT (0.5 wt%) as the inhibitor. The reaction mixture was mechanically stirred at 500 rpm at 70 °C for 24 h under a nitrogen atmosphere. After the reaction, most of the toluene was removed by rotary evaporation at 70 °C, yielding a viscous white liquid. The product was further dried in a vacuum oven at 70 °C for 24 h to obtain the LCO. The chemical structure of the LCO was confirmed by ^{1}H NMR spectroscopy [Supplementary Figure 3].

Fabrication of biphasic rSMP/CB-based flexible strain sensors

The biphasic rSMP/CB strain sensors were prepared by UV curing a homogeneous precursor mixture. First, LCO (0.95 g) and PPDL-DA (0.05 g) were dissolved in DCM (4 mL) in a 15 mL vial. PTME (0.186 g) was then added as the tetrafunctional thiol crosslinker. CB was incorporated at 1 wt% relative to the combined mass of LCO, PPDL-DA, and PTME, while CF-10 was added at a CB:CF-10 mass ratio of 1:1.5. The resulting

CB/CF-10-containing precursor was ultrasonicated using an F-020SD ultrasonic system (Shenzhen Fuyang Technology Group Co., Ltd., China) for 10 min to obtain a homogeneous conductive precursor. Dissolved oxygen was removed by nitrogen bubbling. TPO photoinitiator was then added at 5 wt% relative to the total precursor mass, and the mixture was stirred at 500 rpm at 25 °C for 20 min while protected from light. The precursor was photopolymerized using a 365 nm UV lamp (Zhongshan Xingxuzi Lighting Co., Ltd., China) at an irradiation intensity of 20 mW·cm^{-2} for 10 min. The resulting biphasic rSMP/CB film had a thickness of approximately 0.3 mm. The film was cut into strip sensors or patterned array sensors with initial dimensions of approximately 5 mm × 20 mm before thermomechanical programming.

Reversible actuation programming

The rSMP/CB sensor was thermomechanically programmed to establish stress-free reversible actuation between the high- and low-GF states. For initial thermomechanical programming, the sample was first heated to 140 °C and then stretched to 50% at this temperature. The sample was cooled to 54 °C (T_{mid}) while the imposed deformation was maintained. During cooling through the PPDL crystallization region, oriented PPDL crystallites formed and fixed the programmed alignment within the dual-phase network. After the sample reached 54 °C, the external stress was removed to complete the programming process. Subsequent stress-free cooling from 54 to 22 °C (T_{low}) produced the elongated high-GF state, whereas reheating to 54 °C produced the contracted low-GF state. These two states could be repeatedly accessed by thermal cycling between 22 and 54 °C without repeated mechanical programming. The temperature of 140 °C was used during the initial thermomechanical programming and, when required after extended thermal cycling, as a high-temperature erase/reset condition before reprogramming. Routine reversible GF switching and sensing readout were performed between 22 and 54 °C; 140 °C was not used as a routine GF switching or readout temperature. Unless otherwise specified, GF measurements were performed at 22 °C for the high-GF state and at 54 °C for the low-GF state. When necessary, the reversible actuation state could be re-established by repeating the same thermomechanical programming procedure after the high-temperature erasing step. The 50% pre-strain was applied only during thermomechanical programming and should be distinguished from the subsequent stress-free reversible actuation. After programming, the sensor exhibited an approximately 31% reversible length change between the short state at 54 °C and the elongated state at 22 °C. To evaluate whether the programmed GF states could be restored after cycling-induced attenuation, the cycled sensor was heated to 140 °C to erase the previous programmed state and was then subjected to the same thermomechanical programming procedure. After reprogramming, the GF was re-evaluated at 22 and 54 °C using the same 0%-10% mechanical readout strain range.

Strain sensing measurements

The electromechanical sensing performance of the rSMP/CB sensors and GF-bit arrays was measured using a mechanical stretching system coupled with an electrical resistance measurement system. The sample was fixed between two tensile clamps. Unless otherwise specified, the GF measurements were conducted within a tensile strain range of 0%-10%. The resistance signal was recorded in real time using a Keithley 2450 digital source meter in a two-probe configuration. Copper foil electrodes were attached to both ends of the sample using copper tape.

For temperature-dependent sensing measurements, the sample was placed on a temperature-controlled stage or heated by IR irradiation. The high-GF state was measured at 22 °C. The low-GF state was measured after the sensor-layer temperature was increased through the GF-switching region to approximately 54 °C. For IR photothermal measurements, the sensor-layer temperature was maintained at approximately 54 °C. Unless otherwise specified, quantitative sensing measurements were performed using three independently prepared sensors.

Temperature-dependent GF measurements

To determine the GF-switching window, the electromechanical response was measured over an extended temperature range from 5 to 70 °C. Measurements were performed at 5, 22, 30, 40, 45, 48, 50, 52, 54, 60, and 70 °C, with denser sampling around the switching region. At each temperature, the sample was equilibrated for 5 min before measurement. The GF was determined from the slope of an origin-constrained linear fit to the $\Delta R/R_0$–strain response within the 0%-10% strain range. Unless otherwise specified, data were obtained from $n = 3$ independently prepared sensors and are reported as the mean ± standard deviation (SD).

Thermal switching durability

The cycling durability of the thermally switchable GF states was evaluated by repeatedly switching the sensor between 22 and 54 °C. One complete switching cycle consisted of equilibration at 22 °C, heating to 54 °C, holding until thermal equilibrium was reached, and cooling back to 22 °C. The GF values of the high- and low-GF states were determined at selected cycle numbers over 50 complete thermal cycles. Data were obtained from three independently prepared sensors ($n = 3$) and are reported as the mean ± SD.

GF calculation

The GF of an individual sensing unit was calculated according to the conventional definition for resistive strain sensors[7-9]:

$$\mathrm{GF} = \frac{(R - R_0)/R_0}{\varepsilon}$$

where R_0 is the initial resistance before strain loading, R is the resistance under applied strain, $\Delta R = R - R_0$, and ε is the applied tensile strain. Unless otherwise specified, the GF was obtained from the slope of an origin-constrained linear fit to the $\Delta R/R_0$–strain curve within the 0%-10% strain range.

For real-time sensing measurements, the relative resistance change was calculated as[7-9]

$$\frac{\Delta R}{R_0} = \frac{R(t) - R_0}{R_0}$$

where $R(t)$ is the time-dependent resistance, and R_0 is the baseline resistance before mechanical input.

Effective GF calculation for coded arrays

Following the conventional GF definition[7-9], the effective GF of a coded array was defined from the relative resistance change of the entire array as

$$\mathrm{GF}_{\mathrm{eff}} = \frac{(R_{\mathrm{array}} - R_{\mathrm{array},0})/R_{\mathrm{array},0}}{\varepsilon}$$

where $R_{\mathrm{array},0}$ is the initial resistance of the array, $\Delta R_{\mathrm{array}} = R_{\mathrm{array}} - R_{\mathrm{array},0}$ is the resistance change of the array under strain, and ε is the applied tensile strain. The effective GF was obtained from the slope of the $\Delta R_{\mathrm{array}}/R_{\mathrm{array},0}$–strain curve within the selected strain range. The strain-dependent responses of series-, parallel-, and series–parallel-connected GF-bit arrays were calculated using exact circuit relations based on the measured initial resistance and GF of each constituent unit. For quantitative comparison with experiment, the calculated response was generated over the same 0%-10% strain range, and the calculated effective GF was obtained using the same origin-constrained linear-fitting procedure as for the experimental data. The complete derivation is provided in Supplementary Note 1.

In the coded array, 0 denotes a low-GF unit, whereas 1 denotes a high-GF unit. Before each measurement, the array was thermally addressed into the desired 0/1 coded state, and the overall resistance response was then measured between the common positive and negative electrodes. The exact circuit model for calculating

the strain-dependent response and effective GF of coded arrays, together with its derivation, is provided in Supplementary Note 1.

Electrical connection of GF-bit arrays

The GF-bit arrays were constructed using different electrical connection topologies to achieve multilevel effective GF values. For the 1 × 2 series array, two sensing units were connected in series, and the total resistance was measured between the two outer electrodes. For the 2 × 1 parallel array, two sensing units were connected in parallel between common positive and negative electrodes. For the 1 × 3 series array, three sensing units were connected in series. For the 3 × 1 parallel array, three sensing units were connected in parallel.

For the 3 × 3 array, each row consisted of three sensing units connected in series, and the three rows were further connected in parallel between common positive and negative electrodes. The all-0 state refers to an array in which all units are in the low-GF state, the all-1 state refers to an array in which all units are in the high-GF state, and the mixed 0/1 state refers to an array in which different units are spatially encoded into different GF states. The total resistance and ($\Delta R/R_0$) response of the array were measured between the common positive and negative electrodes.

IR photothermal addressing and temperature measurement

Local photothermal addressing was performed using a 250 W broadband IR light source with a spectral range of 0.76-5 μm. The distance between the light source and the sample surface was 15 cm. During irradiation, the active sensor-layer temperature was monitored using a DLX-HC2508 IR thermometer. Under the selected continuous-irradiation condition, approximately 43 s was required for the active sensing layer to first reach 54 °C. Irradiation was continued as necessary to maintain the sensor within the experimentally identified low-GF temperature plateau. Therefore, 43 s denotes the time required to first reach the representative low-GF readout temperature rather than the total irradiation duration or the final steady-state temperature.

After the IR light source was turned off, the sample was naturally cooled to room temperature to recover the high-GF state. For locally coded arrays, units heated through the experimentally determined GF-switching region and stabilized within the low-GF temperature range were defined as low-GF units, whereas unheated units remaining within the tested low-temperature high-GF regime were defined as high-GF units.

Wearable sensing demonstrations

For the wearable sensing demonstrations, the rSMP/CB sensor was attached to the skin surface of one healthy adult participant. Components A and B of the two-component liquid silicone were mixed at a mass ratio of 1:1, degassed, cast into a mold, and cured at 25 °C for 12 h to obtain a silicone-resin sheet with a thickness of approximately 3 mm. For the demonstration conducted at an active sensor-layer temperature of approximately 54 °C, the cured silicone-resin separation layer was positioned between the active sensing layer and the participant's skin to prevent direct physical contact. The reported temperature of approximately 54 °C therefore refers specifically to the active rSMP/CB sensing layer rather than the skin-contact interface.

Forehead wrinkling and finger flexion were performed voluntarily by the participant while the corresponding resistance responses were recorded. The wearable tests were non-invasive, and the sensor assembly was removed immediately if any discomfort occurred.

Statistical analysis and reproducibility

Unless otherwise specified, quantitative data are presented as the mean ± SD obtained from three independently prepared samples ($n = 3$). For each sensing sample, the GF was determined from the slope of an origin-constrained linear fit to the $\Delta R/R_0$–strain curve within the specified strain range. Representative time-dependent sensing traces are shown where indicated; these experiments were independently repeated at least three times with similar results. The definition of n and the meaning of the error bars are specified in the corresponding figure captions.

RESULTS AND DISCUSSION

We first established the concept of a thermally switchable GF-bit array for programmable gain coding considering the proposed design principle [Figure 1]. A conventional flexible strain sensor has a fixed GF after fabrication; therefore, the same mechanical deformation is always converted into an electrical output with one predetermined gain [Figure 1A]. This fixed-gain response is unsuitable for distributed sensing systems in which weak, intermediate, and strong mechanical signals may coexist. In this case, simply increasing the GF cannot address this issue because a gain that benefits weak-signal detection can over-amplify stronger inputs, whereas a lower gain that stabilizes strong-input readout may lose subtle signals. To overcome this limitation, we define each sensing pixel as a binary GF bit, in which the room-temperature or unheated state represents a high-GF unit, denoted as 1, whereas the thermally switched state represents a low-GF unit, denoted as 0. Here, the binary state refers to the strain-response gain rather than an on/off electrical conductance state; both 0 and 1 units remain mechanically readable sensors. Electrical integration of these local 0/1 gain units allows the array-level effective GF to be programmed by the coding distribution of high- and low-GF pixels. Thus, an all-1 array provides a high effective GF for weak-signal amplification, an all-0 array provides a low effective GF for stable readout of strong inputs, and mixed 0/1 arrays generate intermediate effective GF values for moderate signal windows. The material basis of the GF-bit behavior is the programmed dual-phase structure of the rSMP/CB composite [Figure 1B][19].

In this network, the PPDL crystalline phase primarily acts as a physical alignment frame established during thermomechanical programming, whereas the lower-temperature liquid-crystalline transition provides the reversible stress-free actuation used for GF switching. During operation between 22 and 54 °C, the temperature remains below the principal PPDL melting region. Heating across the lower-temperature transition reduces liquid-crystalline ordering and contracts the programmed sample, producing the low-GF state. Subsequent cooling restores liquid-crystalline ordering and the elongated high-GF state while the PPDL crystalline frame is retained. The accompanying change in matrix configuration alters how the embedded CB conductive network responds to the same applied strain, thereby changing the resistance–strain slope. Thermal stimulation therefore defines the gain state, whereas mechanical strain remains the real-time sensing input. Accordingly, the measured output represents a thermally reconfigured electromechanical gain rather than a simple thermoresistive resistance change. At the device level, a single sensor can be switched from the room-temperature high-GF state to the heated low-GF state by uniform heating, while localized IR irradiation provides a conceptual route to the spatially mixed 0/1 thermal-state coding in an array [Figure 1C]. Under localized irradiation, the target unit was maintained near the representative low-GF readout temperature, whereas the adjacent unit remained below the switching window, supporting thermal contrast between addressed and nonaddressed units [Supplementary Figure 4]. This binary coding strategy can be extended from simple two-pixel units to scalable 3 × 3 arrays, in which increasing the fraction of high-GF pixels gradually increases the effective GF [Figure 1D]. Therefore, Figure 1 summarizes the design used in this study by transforming the GF from a fixed single-device parameter into a discrete, thermally switchable, and electrically combinable array-level gain state. The following sections validate this concept by first demonstrating single-pixel GF switching, then establishing electrical coding in

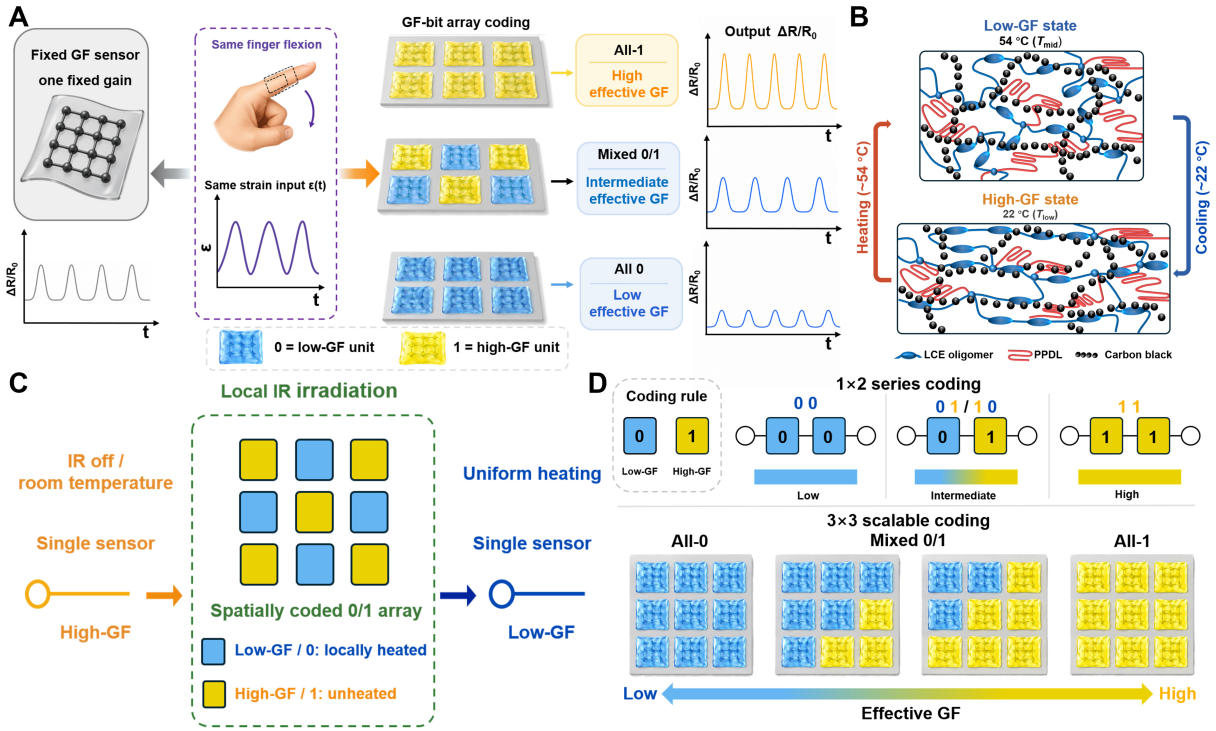


Figure 1. Concept of thermally switchable GF bits for array-level multilevel gain coding. (A) Comparison between a conventional fixed-GF strain sensor and the proposed GF-bit array. Under the same mechanical input, all-1, mixed 0/1, and all-0 arrays generate high, intermediate, and low effective GF outputs, respectively; (B) Schematic mechanism of thermally switchable GF states in the programmed dual-phase rSMP/CB network. Heating across the lower-temperature liquid-crystalline transition drives the contracted low-GF state while the PPDL crystalline framework is retained, whereas cooling restores liquid-crystalline ordering and the elongated high-GF state; (C) Thermal-state coding of single sensors and array pixels. A room-temperature sensor corresponds to the high-GF state, uniform heating switches the sensor to the low-GF state, and local IR irradiation provides a conceptual route to spatially mixed 0/1 thermal-state patterns; (D) Electrical coding from a two-pixel unit to scalable 3 × 3 arrays, showing that increasing the fraction of high-GF pixels increases the array-level effective GF. GF: Gauge factor; rSMP: reversible shape-memory polymer; CB: carbon black; PPDL: poly(pentadecanolide); IR: infrared; LCE: liquid-crystalline elastomer.

small arrays, and finally extending the strategy to multilevel array gain coding and sensing-window matching.

After defining the GF-bit concept, we next examined the thermal and electromechanical behavior of a single rSMP/CB sensing pixel [Figure 2]. The composite was constructed from a programmed dual-phase polymer network containing a liquid-crystalline component, a PPDL crystalline phase, and an embedded CB conductive network prepared with CF-10 as a dispersing additive [Figure 2A]. In the programmed network, the PPDL crystalline phase primarily acts as a physical alignment frame, whereas reversible thermally induced changes in liquid-crystalline ordering drive the stress-free dimensional change used for GF switching. DSC measurements revealed the thermal-transition characteristics of the dual-phase network [Figure 2B]. The 22 and 54 °C markers in Figure 2B denote the selected representative readout temperatures for the high- and low-GF states, respectively; they do not denote material phase-transition onset or peak temperatures. Temperature-dependent electromechanical measurements identify an operational GF-switching interval of approximately 45-54 °C [Supplementary Figure 5], which should be distinguished from the thermal transitions observed by DSC, including PPDL crystallization and melting. During normal operation between 22 and 54 °C, the temperature remains below the principal PPDL melting region, allowing the programmed crystalline frame to be retained. Consistent with this mechanism, the programmed sensor reversibly switches between an elongated high-GF state at 22 °C and a contracted low-GF state at 54 °C, while heating to 140 °C is separately used for the high-temperature erasing/resetting of the programmed state

[Figure 2C]. In Figure 2C, the approximately 21 mm length observed after the 140 °C erase/reset corresponds to the original unprogrammed reference length of the photographed specimen. This value is numerically close to the contracted length of the programmed low-GF state at 54 °C, but the two configurations represent different internal material states. At 54 °C, the programmed PPDL crystalline alignment framework is retained, whereas heating to 140 °C erases the previously programmed alignment. Consequently, the erased specimen cannot be used directly as the low-GF working state and must undergo the 50% stretch–cool–unload thermomechanical programming procedure before the thermally switchable GF states are re-established. Temperature-dependent GF measurements identified three response regimes over the tested temperature range of 5-70 °C [Supplementary Figure 5]. From 5 to approximately 45 °C, the sensor remained in a high-GF regime, although GF decreased modestly with increasing temperature. A substantially steeper decrease occurred over approximately 45-54 °C, identifying this interval as the principal GF-switching region. From 54 to 70 °C, the sensor exhibited a low-GF plateau. The gradual variation observed over the tested 5-45 °C range may be associated with progressive temperature-dependent evolution of liquid-crystalline ordering before the principal switching region is reached. This interpretation is consistent with the dual-phase liquid-crystalline elastomer system reported by Chen *et al.*, in which thermally driven changes in liquid-crystalline ordering are coupled to reversible deformation while the crystalline PPDL phase provides an alignment framework[19]. The electrical response confirmed that this shape-state transition produced a clear GF contrast. Under the same mechanical readout strain, the high-GF state showed a much steeper $\Delta R/R_0$–strain response than the low-GF state, demonstrating that the thermal stimulus acts as the GF-state switching input and that the mechanical strain is used as the sensing readout input [Figure 2D]. Because this comparison is made over the same strain range, the difference in slope directly reflects a gain-state change rather than a change in the applied mechanical input. Quantitatively, the GF increased from 3.3 in the low-GF state to 72.1 in the high-GF state, corresponding to an approximately 22-fold difference [Figure 2E]. Such a large contrast provides a practical separation between the 0 and 1 gain states, which is necessary for reliable array-level coding. Repeated heating–cooling tests showed that the high- and low-GF states remained well separated over the initial 20 thermal switching cycles [Figure 2F]. Extending the test to 50 cycles further confirmed that the two GF states remained clearly distinguishable throughout the complete cycling period [Supplementary Figure 6]. During the later cycles, the high-GF state exhibited a modest downward adjustment, whereas the low-GF state showed only a small upward shift. Nevertheless, the two GF ranges remained clearly separated without overlap, indicating that these limited changes in the characteristic GF levels did not compromise reliable gain-state discrimination. These results support retained sensing functionality and GF-state discrimination under the tested 50-cycle protocol, while also revealing modest cycle-dependent shifts rather than invariant GF values. To examine whether the modest cycle-dependent shifts in GF were accompanied by detectable changes in the bulk polymer network, temperature-sweep oscillatory rheology was performed on rSMP/CB specimens subjected to 0, 20, and 50 prior thermal switching cycles between 22 and 54 °C [Supplementary Figure 7]. During heating from approximately 30 to 110 °C, both the storage modulus (G′) and loss modulus (G″) exhibited pronounced temperature-dependent changes. The specimens subjected to 0, 20, and 50 prior switching cycles showed broadly comparable G′–temperature and G″–temperature profiles over the investigated heating range, suggesting that the characteristic temperature-dependent bulk viscoelastic response of the rSMP/CB network is retained after different prior switching histories. Importantly, the cycle-dependent GF drift observed during the 50-cycle evaluation did not prevent subsequent re-establishment of the programmed gain states. After one 140 °C erase-and-reprogram operation, the measured low- and high-GF values were 3.35 and 73.9, respectively, close to their corresponding initial values of 3.3 and 72.1, thereby recovering an approximately 22-fold GF contrast [Supplementary Table 2]. This post-cycling result demonstrates erasability and reprogrammability of the programmed GF-bit states under the tested protocol and identifies erase-and-reprogramming as a feasible route for refreshing the programmed gain contrast after cycling-induced drift. In addition, IR irradiation increased the sensor-layer temperature through the GF-switching region to approximately 54 °C

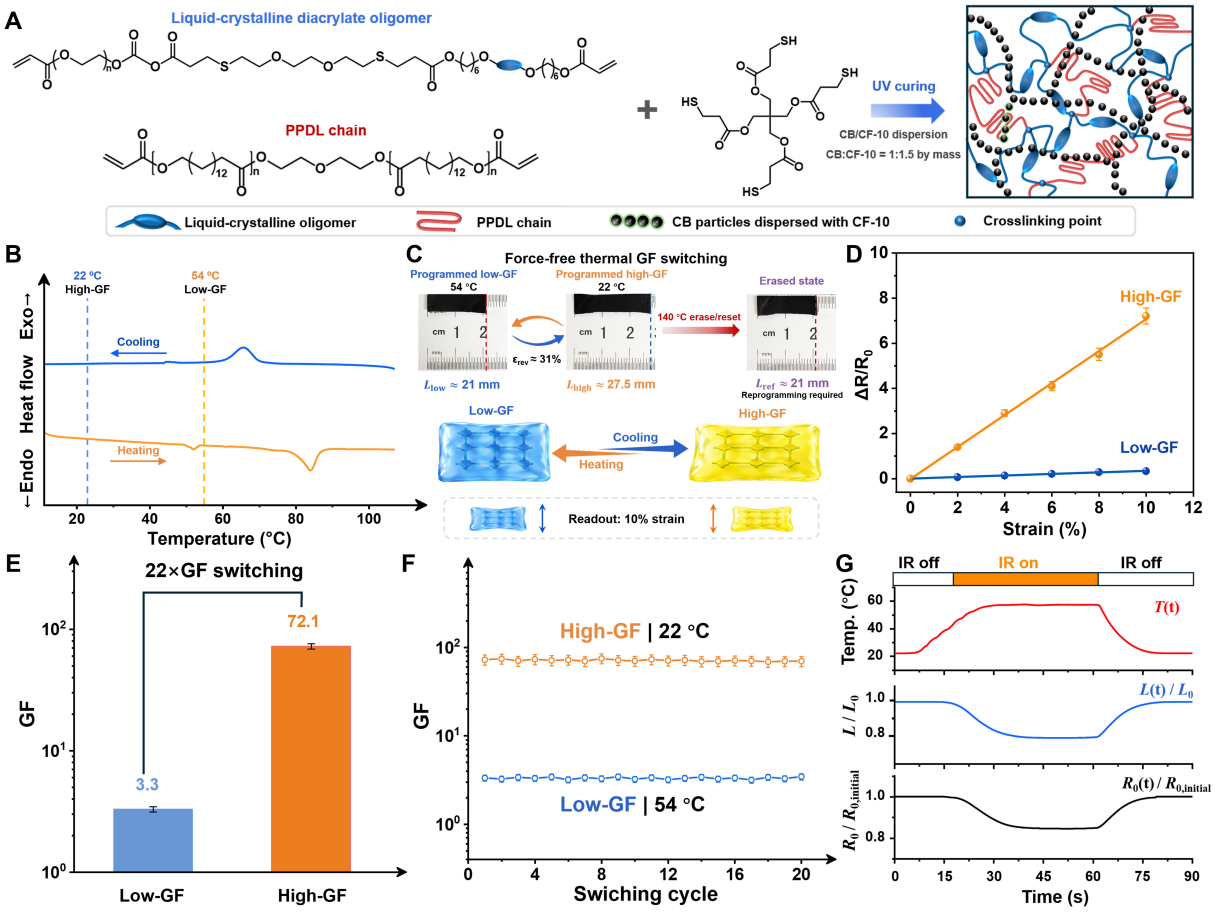


Figure 2. Single-pixel thermally switchable GF bit based on an rSMP/CB composite. (A) Material design of the programmed dual-phase rSMP/CB network containing the liquid-crystalline component, PPDL crystalline phase, and CB conductive fillers prepared with CF-10 as a dispersing additive; (B) DSC heating and cooling curves of the dual-phase network. The vertical dashed lines at 22 and 54 °C mark the representative high- and low-GF readout temperatures, respectively, rather than material phase-transition onset or peak temperatures. The operational GF-switching interval of approximately 45-54 °C was identified separately from temperature-dependent electromechanical measurements [Supplementary Figure 5]; (C) Reversible thermal switching of the programmed sensor between the contracted low-GF state at 54 °C and the elongated high-GF state at 22 °C after thermomechanical programming. The 50% pre-strain is applied only during programming, whereas the subsequent stress-free reversible actuation is approximately 31%. The approximately 21 mm length observed after the 140 °C erase/reset corresponds to the restored unprogrammed reference length of the photographed specimen. Although this length is numerically close to that of the programmed low-GF state at 54 °C, the two configurations represent physically different internal states: the programmed PPDL crystalline alignment is retained at 54 °C but erased at 140 °C, after which thermomechanical reprogramming is required to re-establish the switchable GF states; (D) $\Delta R/R_0$–strain responses of the sensor in the low- and high-GF states; (E) GF comparison between the two states; (F) Repeated thermal switching of the high- and low-GF states over the initial 20 heating–cooling cycles. Extended cycling behavior up to 50 cycles is provided in Supplementary Figure 6; (G) IR-triggered photothermal response and corresponding length change, demonstrating photothermal access to the low-GF state. Data in (E and F) are presented as the mean ± SD (n = 3 independently prepared sensors). The time-dependent traces in (G) are representative of three independently repeated measurements. GF: Gauge factor; rSMP: reversible shape-memory polymer; CB: carbon black; PPDL: poly(pentadecanolide); DSC: differential scanning calorimetry; IR: infrared; SD: standard deviation; UV: ultraviolet.

and produced a corresponding reversible length change, demonstrating that broadband IR photothermal heating can externally access the representative low-GF state [Figure 2G]. The sensor-layer temperature reached approximately 54 °C within 43 s under the selected IR irradiation condition [Supplementary Figure 8]. These results identify the single rSMP/CB pixel as a thermally switchable GF bit and provide a basis for the electrical coding of multiple GF bits.

After confirming the single-pixel GF bit, we next examined whether multiple thermally switchable gain units could be electrically combined to generate discrete array-level effective GF outputs. We first constructed 1 ×

2 series-connected GF-bit units with four binary codes: 00, 01, 10, and 11 [Figure 3A]. Here, 0 denotes the heated low-GF state and 1 denotes the room-temperature high-GF state. Under the same mechanical readout strain, the 00 code produced the lowest resistance-response slope, the 11 code produced the highest slope, and the mixed 01/10 codes generated intermediate responses [Figure 3B]. The extracted effective GF values followed the same trend, confirming that the local binary GF states can be converted into a stepwise array-level gain output through electrical integration [Figure 3C]. The mixed 0/1 code therefore represents the simplest intermediate-gain state generated by combining two binary GF bits. The similar responses of the 01 and 10 states also indicate that, in a symmetric series configuration, the effective gain is mainly determined by the number of high-GF units rather than their order. This behavior is expected for a nearly symmetric series unit, where the two pixels additively contribute to the total resistance change. Repeated switching among 00, 01, and 11 codes further verified that the two-bit unit can be reversibly coded and read out without reconstructing the device architecture [Figure 3D]. Next, the two-bit coding strategy was extended to 2 × 1 parallel-connected GF-bit units to examine the role of electrical topology [Figure 3E]. Similar to the series configuration, the parallel units showed distinguishable low, intermediate, and high resistance-response slopes for the 00, mixed 0/1, and 11 codes, respectively [Figure 3F]. The corresponding effective GF values increased stepwise with the fraction of high-GF units, demonstrating that binary GF states can be translated into multilevel gain outputs not only in series circuits but also in parallel electrical configurations [Figure 3G]. Although the absolute effective GF differs between series and parallel topologies, both configurations preserve the same low-to-high gain hierarchy from 00 to mixed 0/1 and 11 states. These results establish the basic electrical coding rule of GF bits and indicate the possibility of scaling the strategy from two-bit units to larger arrays.

Having established two-bit electrical coding, we next examined whether the GF-bit strategy could be scaled to larger arrays and whether the resulting effective GF could be quantitatively rationalized [Figure 4]. This is important because the GF-bit concept is useful only if local binary gain states remain distinguishable after electrical integration into larger and more complex arrays. To evaluate such systems, we first constructed 1 × 3 series-connected GF-bit arrays with different binary codes [Figure 4A]. Increasing the number of high-GF units progressively increased the effective GF, confirming that local 0/1 gain states can be combined into multilevel outputs in a series topology. We next evaluated 3 × 1 parallel-connected arrays [Figure 4B]. Despite the different electrical topology, the effective GF again increased with the fraction of high-GF units, showing that the coding strategy is not limited to a specific circuit configuration. To further demonstrate scalability, we fabricated 3 × 3 GF-bit arrays with different distributions of low- and high-GF units [Figure 4C]. Under the same mechanical readout strain, these arrays exhibited distinct $\Delta R/R_0$–strain slopes, with higher fractions of high-GF units producing larger resistance responses [Figure 4D].

Because the readout strain is unchanged, these different slopes arise from the programmed GF-bit distribution rather than from differences in mechanical loading. The measured array-level effective GF values were 4.4, 32.0, 51.5, and 76.2 for states a-d, respectively, corresponding to 0/9 (all-0), 3/9, 6/9, and 9/9 (all-1) high-GF units in the specific configurations shown in Figure 4C-E. These results indicate that local binary states can be converted into graded array-level gain outputs. To rationalize this behavior, we developed a finite-strain circuit model based on the fitted local GF values, measured initial resistances, and exact series/parallel circuit relations of the constituent GF-bit units [Figure 4F and Supplementary Note 1]. The calculated effective GF was then obtained from an origin-constrained linear fit to the calculated $\Delta R/R_0$–strain response over the same 0%-10% strain range used experimentally. The calculated effective GF values followed the measured values across the series, parallel, and 3 × 3 array configurations [Figure 4G]. The observed deviations are likely associated with unit-to-unit resistance variation, electrode/contact resistance, and small differences in thermal-state switching among pixels. Moreover, the measured effective GF systematically increased with the fraction of high-GF units across different array topologies [Figure 4H].

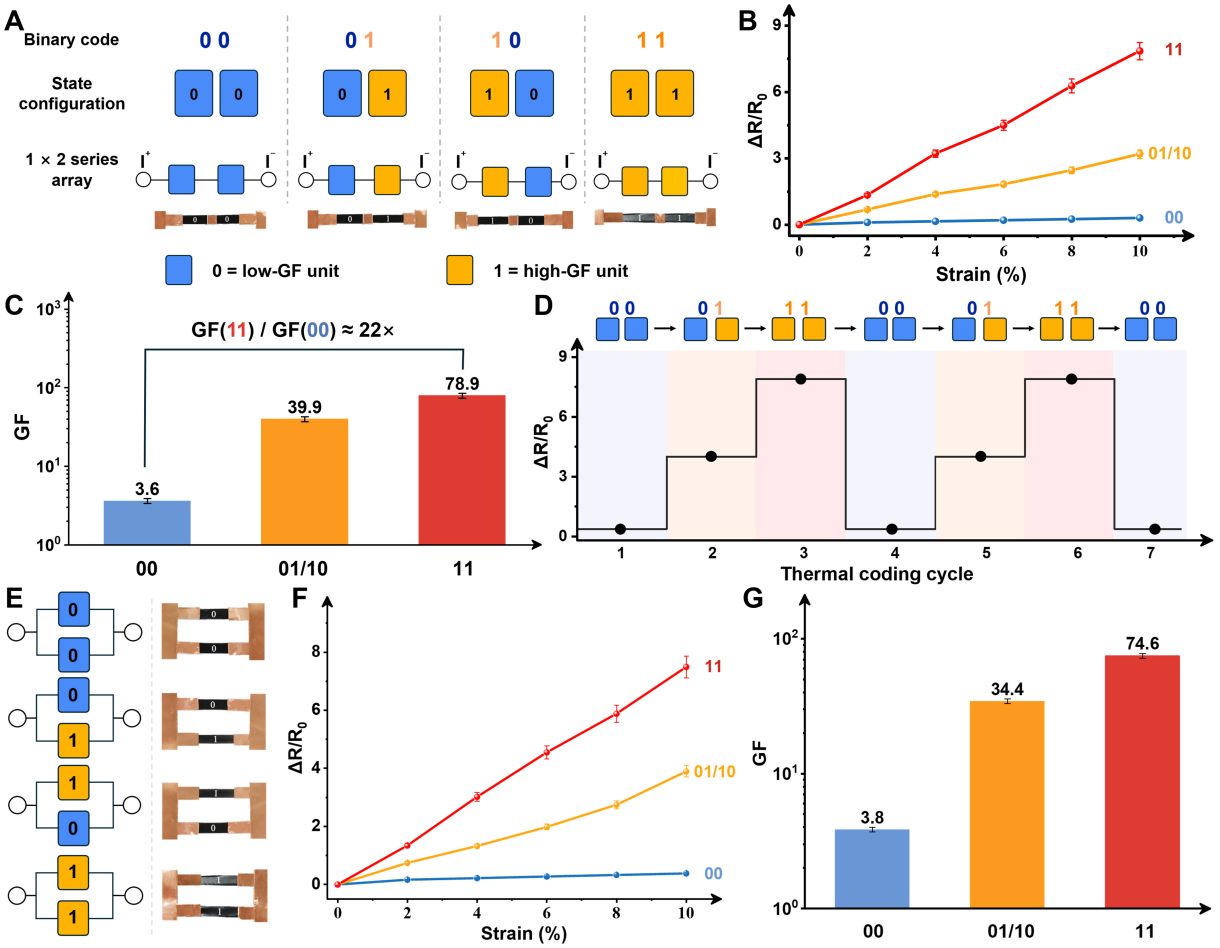


Figure 3. Two-bit electrical coding of thermally switchable GF units. (A) Schematic and photographs of 1 × 2 series-connected GF-bit units with 00, 01, 10, and 11 codes; (B and C) Strain-dependent resistance responses and extracted effective GF values of the series-connected units, showing stepwise gain modulation from 00 to mixed 0/1 and 11 states; (D) Reversible coding/readout sequence of the series-connected GF-bit unit; (E) Schematic and photographs of 2 × 1 parallel-connected GF-bit units representing the 00, mixed 01/10, and 11 codes; (F and G) Strain-dependent resistance responses and extracted effective GF values of the parallel-connected units, demonstrating electrical-topology-dependent multilevel gain coding. GF values are presented as the mean ± SD (n = 3 independently prepared two-pixel arrays). GF: Gauge factor; SD: standard deviation.

To distinguish the effect of a high-GF fraction from that of the spatial arrangement, we further compared 3 × 3 arrays containing the same number of high-GF units but exhibiting different spatial distributions [Supplementary Figure 9]. The resulting effective GF values differed only slightly within the range of experimental variation, indicating that, for the present array with approximately balanced unit resistances, the high-GF fraction is the primary determinant of the effective GF, whereas spatial arrangement provides only a secondary contribution. This monotonic relationship provides the direct experimental basis for converting binary 0/1 GF states into programmable multilevel gain outputs. Together, these results show that GF-bit arrays can be scaled and quantitatively rationalized across different electrical topologies, providing a basis for selecting effective GF values according to the mechanical signal window.

After establishing scalable and model-rationalized GF-bit array coding, we examined sensing-window matching under controlled thermal and photothermal conditions [Figure 5]. The purpose of this demonstration is to evaluate whether different GF states can be selected for mechanical inputs with different amplitudes, rather than to define 54 °C as a temperature for prolonged direct skin exposure. The 22 and 40 °C measurements represent low- and mildly elevated-temperature conditions in which the high-GF state

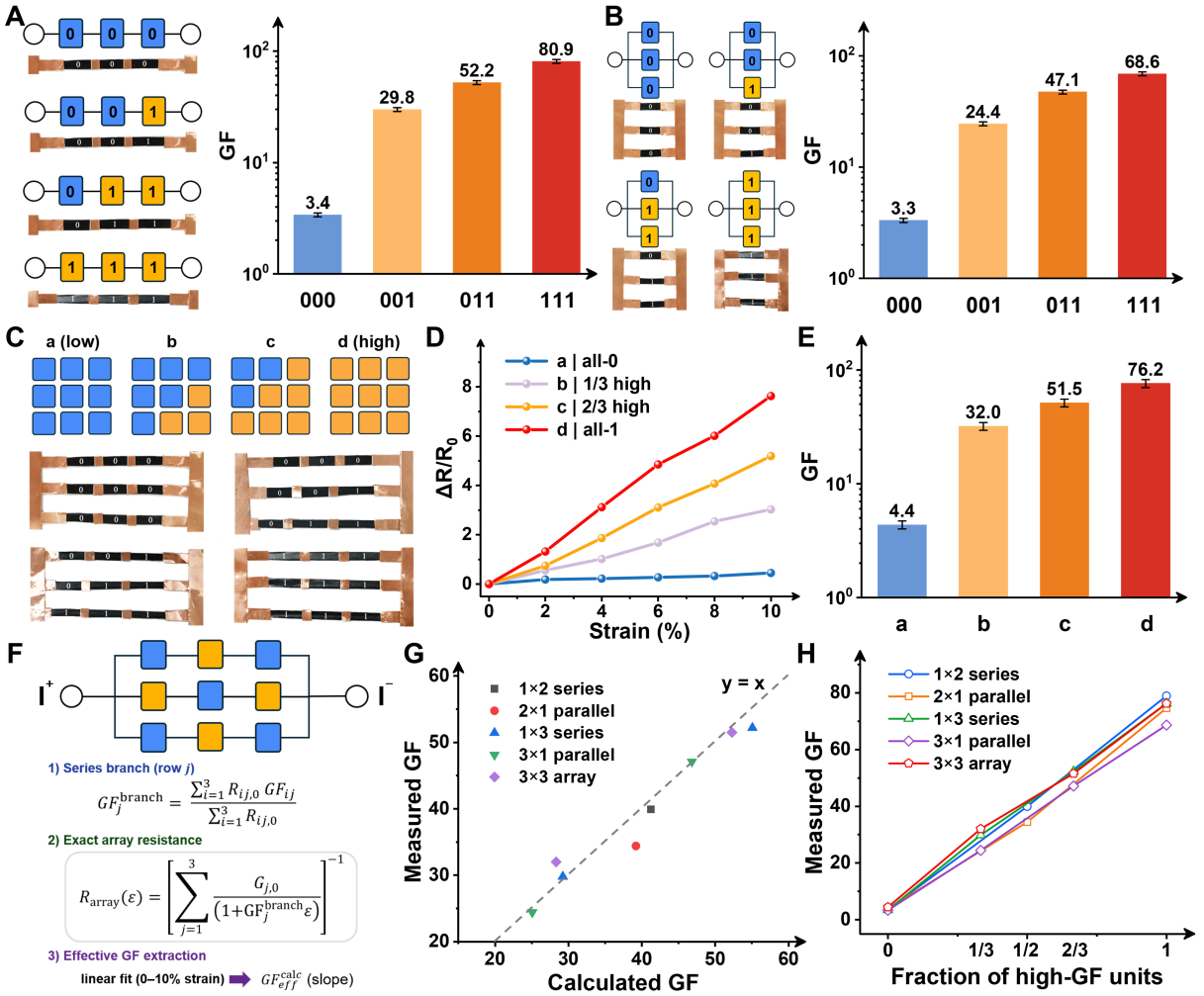


Figure 4. Scalable GF-bit array coding and model-rationalized effective GF outputs. (A) Coding configurations and extracted effective GF values of 1 × 3 series-connected GF-bit arrays; (B) Coding configurations and extracted effective GF values of 3 × 1 parallel-connected GF-bit arrays; (C) Four representative 3 × 3 coding states, with blue denoting the low-GF state (0) and orange denoting the high-GF state (1). Reading each row from left to right and the rows from top to bottom, states a-d are 000/000/000, 000/001/011, 001/011/111, and 111/111/111, respectively. These states contain 0, 3, 6, and 9 high-GF units out of 9; (D and E) Corresponding resistance-strain responses and measured array-level effective GF values of 4.4 (a, all-0), 32.0 (b, 1/3 high-GF), 51.5 (c, 2/3 high-GF), and 76.2 (d, all-1), respectively. Each row contains three units in series, and the three rows are connected in parallel; (F) Finite-strain circuit model based on the fitted unit-level GF values, measured initial resistances, and exact series/parallel circuit relations; (G) Comparison between the circuit-model calculations and measured effective GF values for different array configurations; (H) Measured effective GF as a function of the fraction of high-GF units, showing binary-to-multilevel gain coding across series, parallel, and 3 × 3 arrays. The measured GF values are presented as the mean ± SD (n = 3 independently prepared arrays). GF: Gauge factor; SD: standard deviation.

is retained, whereas 54 °C is used as a controlled proof-of-concept sensor-layer temperature for accessing the low-GF state. Therefore, temperature serves as the GF-state control input, while deformation or contact is the mechanical sensing input. In the skin-mounted configuration, the rSMP/CB sensing layer was integrated with a layered structure containing a thermal-protective layer between the active sensing layer and the skin, such that external irradiation increased the sensor-layer temperature without direct contact between the heated sensing layer and the skin [Figure 5A]. This configuration was designed to separate the roles of the two inputs, wherein temperature controls the GF state and mechanical deformation or contact provides the sensing input. During repeated heating–cooling cycles, the sensor switches between the high- and low-GF states as the temperature crosses the GF-switching window, without changing the device architecture [Figure 5B]. We first evaluated whether the sensor could maintain its mechanical readout during different thermal

stages. At 22 °C, the high-GF state clearly resolved weak forehead-wrinkling deformation, demonstrating the advantage of high gain for subtle signals [Figure 5C]. When the sensor was maintained at 40 °C, below the GF-switching threshold, the high-GF state was preserved and could identify finger flexion deformation [Figure 5D]. The 40 °C result shows that mild heating within the tested high-GF regime does not switch the sensor into the low-GF state. By contrast, when the active sensing layer was brought to approximately 54 °C under controlled thermal conditions, the sensor entered and maintained the low-GF state. During this proof-of-concept wearable demonstration, the active sensing layer was separated from the participant's skin by the approximately 3 mm cured 404A/404B silicone-resin layer. The stated temperature refers to the active sensing layer rather than the skin-side interface. Because the skin-side interface temperature was not independently measured, no quantitative claim regarding the skin-contact temperature is made. The low-GF state produced a lower-amplitude mechanical response during finger flexion [Figure 5E] and maintained a stable resistance response over the tested strain range of 0%-30% [Supplementary Figure 10]. We next used a nominal repeated normal-contact protocol to compare low-, intermediate-, and high-effective-GF arrays [Figure 5F and G]. The all-0 array produced the lowest output amplitude, the mixed 0/1 array produced an intermediate output, and the all-1 array produced the largest output. These results demonstrate selectable output-amplitude windows through array-level GF coding rather than simple maximization of GF. The selectable gain states enable the array response to be matched to different expected mechanical-signal amplitude ranges. Related skin-interfaced thermal, photothermal, compression, and electronic-skin systems illustrate application settings in which thermal and mechanical inputs may coexist[40-42]. Potential applications of the GF-bit concept include wearable motion monitoring, electronic skins, distributed robotic skins, and soft human–machine interfaces containing mechanical signals with different amplitudes. However, the present 54 °C condition should be regarded as a proof-of-concept active sensor-layer temperature. Shifting the GF-switching window toward a physiologically comfortable temperature range remains necessary for prolonged skin-contact applications.

More specifically, the practical distinction between the GF-bit architecture and a conventional fixed-GF sensor lies in selectable gain-window matching rather than in maximizing GF alone. Whereas a fixed-GF sensor provides only one electromechanical gain after fabrication, the same GF-bit sensing platform can access low-, intermediate-, and high-array-level gain states through local thermal-state assignment and electrical combination, without requiring a separately fabricated sensor for each gain window. For the specific 3 × 3 configurations shown in Figure 4C-E, the measured effective GF values were approximately 4.4, 32.0, 51.5, and 76.2 for the all-0, 1/3-high-GF, 2/3-high-GF, and all-1 coding states, respectively, under nominally matched mechanical-input conditions. Accordingly, high-gain states can be selected for weak deformation such as subtle motion or light contact, intermediate-gain states for moderate joint or tactile inputs, and low-gain states for larger bending or stronger contact inputs requiring a more moderate output amplitude. At the framework level, GF-bit coding is defined by functional requirements rather than by a particular polymer formulation: the sensing elements must provide reproducibly distinguishable and switchable local GF states that can be discretized and electrically combined. Thermally reversible matrix behavior has also been demonstrated in crosslinked polyurethane networks containing poly(ε-caprolactone) (PCL) segments of different molecular weights and in poly(octylene adipate) (POA)/PCL cocrystalline networks[20,43]. These systems provide credible alternative matrix platforms for future GF-bit implementations when integrated with a suitable conductive phase and experimentally established switchable GF states. Because the circuit model developed here uses the measured initial resistance and GF of each sensing unit and has been validated in series, parallel, and series–parallel topologies, the array-coding framework is not restricted to the specific rSMP/CB formulation demonstrated in this study. The present system therefore represents a material realization of a broader strategy for converting switchable local sensitivity states into programmable multilevel array gain.

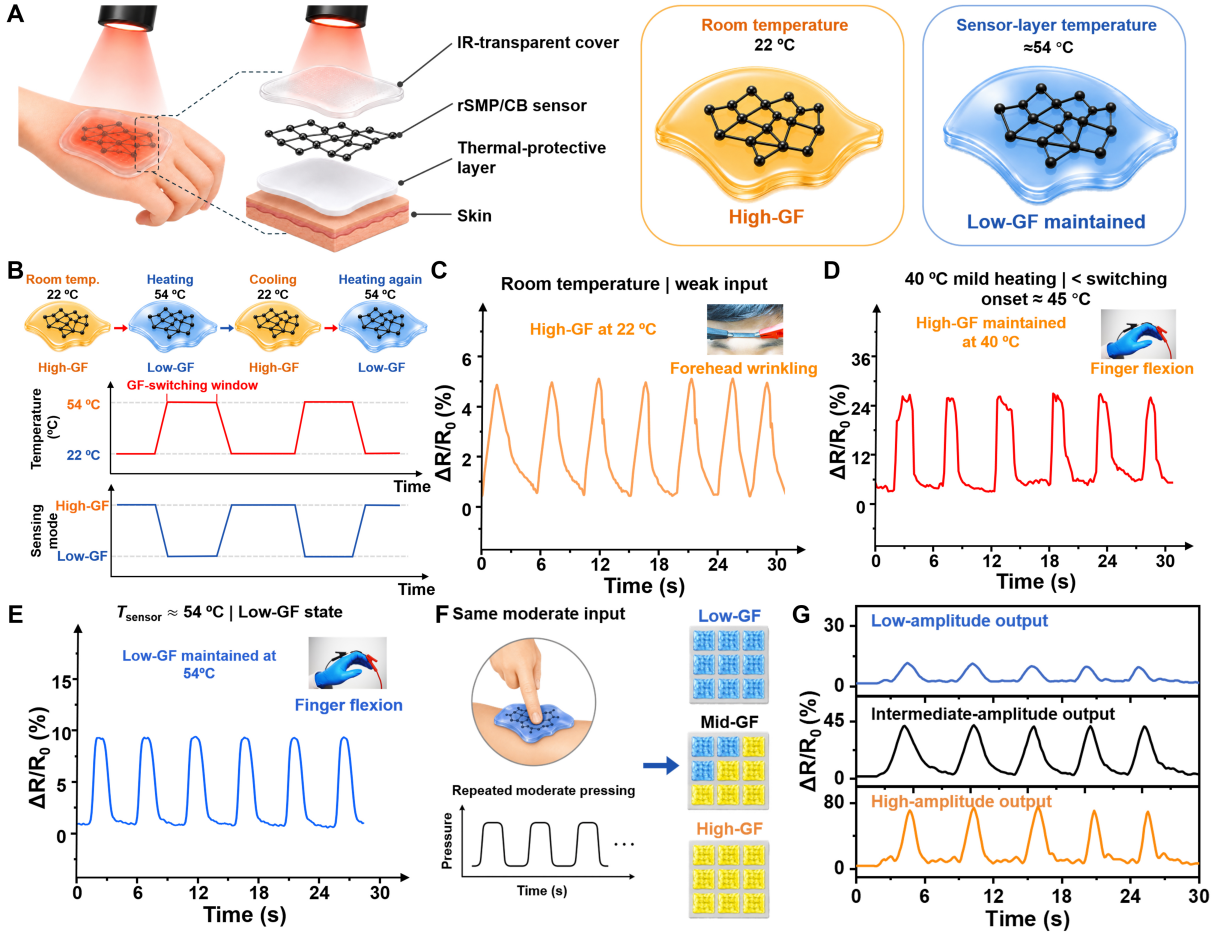


Figure 5. Thermal-state-controlled sensing-window matching under simulated photothermal/thermal elevation conditions. (A) Schematic of the layered skin-mounted configuration. For the approximately 54 °C active sensor-layer condition, a cured 404A/404B silicone-resin separation layer with a thickness of approximately 3 mm was positioned between the rSMP/CB sensing layer and the participant's skin to prevent direct contact with the heated sensing layer. The stated temperature refers to the active sensing layer rather than the skin-side interface; (B) Reversible thermal switching of the GF state during repeated heating–cooling cycles; (C) High-GF readout of weak forehead-wrinkling deformation at 22 °C; (D) High-GF response maintained at 40 °C, below the GF-switching threshold, showing that mild heating does not trigger the low-GF state; (E) Low-GF finger-flexion readout with the active rSMP/CB sensing layer maintained at approximately 54 °C and separated from the skin by the 3 mm silicone-resin layer; (F) Pressing-induced normal-contact input used to evaluate contact-signal window matching; (G) Representative resistance responses of low-, intermediate-, and high-effective-GF arrays under the same nominal contact-input protocol. The coded arrays produce progressively increasing output amplitudes from the low- to intermediate- and high-effective-GF states. The photographs in (C-E) were taken by the authors during the reported experiments. rSMP: Reversible shape-memory polymer; CB: carbon black; GF: gauge factor.

Limitations of the study

The present study establishes the GF-bit strategy as a proof-of-concept using rSMP/CB sensing units and arrays up to 3 × 3 under a tested 50-cycle thermal switching protocol. The current 54 °C low-GF condition is a representative active sensor-layer readout temperature for the low-GF state and should be shifted toward a lower operating range for prolonged skin-contact applications. Future development will focus on longer-term switching operation, independent thermal addressing in larger arrays, and experimental implementation of the functionally defined GF-bit framework in other material systems providing reproducibly distinguishable and switchable local GF states.

CONCLUSION

We demonstrated a thermally switchable GF-bit strain-sensing system based on a programmed dual-phase shape-memory polymer/CB composite. Thermal actuation changes the polymer shape state and the

strain-dependent response of the CB network, whereas mechanical strain provides the sensing readout input. A single sensing pixel exhibited high- and low-GF states of 72.1 and 3.3, respectively, corresponding to an approximately 22-fold difference. Temperature-dependent measurements identified a high-GF regime over the tested range of 5-45 °C, a principal GF-switching region over approximately 45-54 °C, and a low-GF plateau over the tested range of 54-70 °C. The 22 and 54 °C conditions serve as representative readout temperatures for the high- and low-GF states, respectively, rather than material phase-transition onset or peak temperatures. The two GF states remained distinguishable over the tested 50-cycle thermal switching interval, although gradual cycle-dependent shifts in the characteristic GF levels became evident during later cycles. Temperature-sweep rheological measurements on specimens subjected to 0, 20, and 50 prior switching cycles showed broadly comparable temperature-dependent storage- and loss-modulus profiles, supporting retention of the characteristic bulk viscoelastic response under the tested preconditioning histories. In a representative recovery test, high-temperature erasing followed by thermomechanical reprogramming restored the attenuated GF states to values close to their initial levels, supporting post-cycling erasability and reprogrammability of the programmed GF states under the tested protocol. At the array level, local binary GF states were integrated into series, parallel, and 3 × 3 configurations to generate discrete effective-GF outputs. The measured array-level trends were rationalized using a finite-strain circuit model based on fitted unit-level GF values, measured initial resistances, and exact series/parallel circuit relations. The resulting low-, intermediate-, and high-effective-GF states provide selectable output windows under nominally matched mechanical-input protocols. Together, these results establish GF as a thermally switchable and electrically combinable material-state gain variable for programmable flexible sensor arrays.

DECLARATIONS

Authors' contributions

Methodology, investigation, data curation, visualization, and writing - original draft: Qiao, W.; Wang, Z.
Investigation, data acquisition, and data curation: Zhu, X.; Dong, L.; Yang, C.; Wang, Y.
Formal analysis and data interpretation: Cui, H.
Writing, review, and editing: Wang, T.
Conceptualization, supervision, funding acquisition, writing - original draft, writing - review, and editing: Zhang, X.
Conceptualization, supervision, project administration, writing - review and editing: Kong, J.
All authors read and approved the final manuscript.

Availability of data and materials

The original contributions presented in this study are included in the article and Supplementary Materials. Further inquiries can be directed to the corresponding author(s).

AI and AI-assisted tools statement

During the preparation of this manuscript, the AI tool ChatGPT (version GPT-5.5, released 2026-04-23), developed by OpenAI, was used solely for language editing. The tool did not influence the study design, data collection, analysis, interpretation, or the scientific content of the work. All authors take full responsibility for the accuracy, integrity, and final content of the manuscript.

Financial support and sponsorship

This work was supported by the National Natural Science Foundation of China (Nos. 52373120 and 52003220), National Science Fund for Distinguished Young Scholars (No. 2025034), and Aoxiang Rising Star Program of Northwestern Polytechnical University (Nos. 24SH0201283 and 24GH0201283). The funders had no role in study design, data collection, analysis, interpretation, or manuscript preparation.

Conflicts of interest

All authors declared that there are no conflicts of interest.

Ethical approval and consent to participate

This study involved only non-invasive data collection using externally attached flexible strain sensors during routine voluntary forehead wrinkling, finger flexion, and controlled contact-input demonstrations. The procedures did not involve invasive interventions or human health risks. According to Article 32 of the "Measures for the Ethical Review of Life Science and Medical Research Involving Human Subjects (Trial)", this study meets the conditions for exemption from ethical review. All participants participated in the experiment with informed consent.

Consent for publication

Not applicable.

Copyright

© The Author(s) 2026.

Supplementary Materials

Supplementary Materials

REFERENCES

1. Ates, H. C.; Nguyen, P. Q.; Gonzalez-Macia, L.; et al. End-to-end design of wearable sensors. *Nat. Rev. Mater.* **2022**, *7*, 887-907. DOI PubMed PMC
2. Xu, C.; Yang, Y.; Gao, W. Skin-interfaced sensors in digital medicine: from materials to applications. *Matter* **2020**, *2*, 1414-45. DOI PubMed PMC
3. Xu, Z.; Zhang, C.; Wang, F.; et al. Smart textiles for personalized sports and healthcare. *Nanomicro. Lett.* **2025**, *17*, 232. DOI PubMed PMC
4. Qu, J.; Cui, G.; Li, Z.; et al. Advanced flexible sensing technologies for soft robots. *Adv. Funct. Mater.* **2024**, *34*, 2401311. DOI
5. Gong, S.; Lu, Y.; Yin, J.; Levin, A.; Cheng, W. Materials-driven soft wearable bioelectronics for connected healthcare. *Chem. Rev.* **2024**, *124*, 455-553. DOI PubMed
6. Zhang, Y.; Zheng, X. T.; Zhang, X.; Pan, J.; Thean, A. V. Hybrid integration of wearable devices for physiological monitoring. *Chem. Rev.* **2024**, *124*, 10386-434. DOI PubMed
7. Zhao, S.; Liu, D.; Yan, F. Wearable resistive-type stretchable strain sensors: materials and applications. *Adv. Mater.* **2025**, *37*, e2413929. DOI PubMed
8. Liu, Z.; Zhu, T.; Wang, J.; et al. Functionalized fiber-based strain sensors: pathway to next-generation wearable electronics. *Nano. Micro. Lett.* **2022**, *14*, 806. DOI PubMed PMC
9. Zhao, W.; Lin, Z.; Sun, Z.; et al. Road narrow-inspired strain concentration to wide-range-tunable gauge factor of ionic hydrogel strain sensor. *Adv. Sci.* **2023**, *10*, e2303338. DOI PubMed PMC
10. Xu, B.; Yang, M.; Cheng, W.; et al. Precision aerosol-jet micropatterning of liquid metal for high-performance flexible strain sensors. *Nat. Commun.* **2025**, *16*, 7920. DOI PubMed PMC
11. Meng, Q.; Chi, T.; Guo, S.; et al. Highly sensitive strain sensors with ultra-low detection limit based on pre-defined serpentine cracks. *Mater. Horiz.* **2025**, *12*, 178-89. DOI PubMed
12. Tan, C.; Dong, Z.; Li, Y.; et al. A high performance wearable strain sensor with advanced thermal management for motion monitoring. *Nat. Commun.* **2020**, *11*, 3530. DOI PubMed PMC
13. Yang, H.; Ding, S.; Wang, J.; et al. Computational design of ultra-robust strain sensors for soft robot perception and autonomy. *Nat. Commun.* **2024**, *15*, 1636. DOI PubMed PMC
14. Oh, H.; Yi, G. C.; Yip, M.; Dayeh, S. A. Scalable tactile sensor arrays on flexible substrates with high spatiotemporal resolution enabling slip and grip for closed-loop robotics. *Sci. Adv.* **2020**, *6*, eabd7795. DOI PubMed PMC
15. Su, Q.; Zou, Q.; Li, Y.; et al. A stretchable and strain-unperturbed pressure sensor for motion interference-free tactile monitoring on skins. *Sci. Adv.* **2021**, *7*, eabi4563. DOI PubMed PMC
16. Tan, X. C.; Xu, J. D.; Jian, J. M.; et al. Programmable sensitivity screening of strain sensors by local electrical and mechanical properties coupling. *ACS. Nano.* **2021**, *15*, 20590-9. DOI PubMed
17. Bai, Y.; Zhou, Y.; Wu, X.; et al. Flexible strain sensors with ultra-high sensitivity and wide range enabled by crack-modulated electrical pathways. *Nanomicro. Lett.* **2024**, *17*, 64. DOI PubMed PMC
18. Lee, S.; Lee, Y.; Park, C.; et al. Shape-reconfigurable crack-based strain sensor with ultrahigh and tunable sensitivity. *Adv. Funct. Mater.* **2025**, *35*, 2421812. DOI

19. Chen, G.; Jin, B.; Shi, Y.; Zhao, Q.; Shen, Y.; Xie, T. Rapidly and repeatedly reprogrammable liquid crystalline elastomer via a shape memory mechanism. *Adv. Mater.* **2022**, *34*, e2201679. DOI PubMed
20. Huang, Y.; Dang, G.; Zhu, M.; Fan, L.; Rong, M.; Zhang, M. External stress-free reversible multiple shape memory polymer enabled by using broad melting range as equivalent multiple switching phases. *Appl. Mater. Today.* **2023**, *30*, 101709. DOI
21. Bruining, T.; Tomé, D. R.; Liu, D. Shape programming of liquid crystal elastomers by two-stage wavelength-selective photopolymerization. *Mater. Horiz.* **2026**, *13*, 243-51. DOI PubMed PMC
22. Li, Y.; Tang, H. H.; Luo, Y. C.; et al. Reversible stepless multiple shape memory polymer comprising amorphous region as switching phase. *Adv. Funct. Mater.* **2025**, *35*, 2500230. DOI
23. Kim, S.; Lee, D.; Bae, S.; et al. Thermal rectification of shape memory polymer composites by programmable conductivity modulation. *Mater. Horiz.* **2026**, *13*, 3993-4002. DOI PubMed
24. Li, M.; Chen, S.; Fan, B.; Wu, B.; Guo, X. Printed flexible strain sensor array for bendable interactive surface. *Adv. Funct. Mater.* **2020**, *30*, 2003214. DOI
25. Song, X.; Gu, Y.; Wang, S.; et al. Scalable integration of high sensitivity strain sensors based on silicon nanowire spring array directly grown on flexible polyimide films. *Nano. Lett.* **2025**, *25*, 2290-7. DOI PubMed
26. Wang, S.; Chen, X.; Li, S.; et al. Advances in micro/nano-engineered flexible sensor arrays for intelligent human-machine interaction. *Soft. Sci.* **2025**, *5*, 28. DOI
27. Wei, Y.; Pan, F.; Lin, X.; Zhang, L.; Xiang, J.; Chen, Y. On-demand reprogrammable mechanical metamaterial driven by structure performance relations. *Adv. Mater.* **2025**, *37*, e2410865. DOI PubMed
28. Yan, W.; Fuh, H. R.; Lv, Y.; et al. Giant gauge factor of Van der Waals material based strain sensors. *Nat. Commun.* **2021**, *12*, 2018. DOI PubMed PMC
29. Zhou, X.; Zhang, X.; Zhao, H.; Krishnan, B. P.; Cui, J. Self-healable and recyclable tactile force sensors with post-tunable sensitivity. *Adv. Funct. Mater.* **2020**, *30*, 2003533. DOI
30. Liu, H.; Du, C.; Liao, L.; et al. Approaching intrinsic dynamics of MXenes hybrid hydrogel for 3D printed multimodal intelligent devices with ultrahigh superelasticity and temperature sensitivity. *Nat. Commun.* **2022**, *13*, 3420. DOI PubMed PMC
31. Li, M.; Pu, J.; Cao, Q.; et al. Recent advances in hydrogel-based flexible strain sensors for harsh environment applications. *Chem. Sci.* **2024**, *15*, 17799-822. DOI PubMed PMC
32. Wu, S.; Kim, D.; Tang, X.; King, M. W.; Zhu, Y. Encapsulated stretchable amphibious strain sensors. *Mater. Horiz.* **2024**, *11*, 5070-80. DOI PubMed PMC
33. Wu, X. P.; Luo, X. M.; Chen, H. L.; et al. Fatigue crack-based strain sensors achieving flow detection and motion monitoring for reconnaissance robot applications. *Mater. Horiz.* **2024**, *11*, 4207-22. DOI PubMed
34. Zhu, J.; Wu, X.; Jan, J.; Du, S.; Evans, J.; Arias, A. C. Tuning strain sensor performance via programmed thin-film crack evolution. *ACS. Appl. Mater. Interfaces.* **2021**, *13*, 38105-13. DOI PubMed
35. Xia, Y.; He, Y.; Zhang, F.; Liu, Y.; Leng, J. A review of shape memory polymers and composites: mechanisms, materials, and applications. *Adv. Mater.* **2021**, *33*, e2000713. DOI PubMed
36. Wan, X.; Xiao, Z.; Tian, Y.; et al. Recent advances in 4D printing of advanced materials and structures for functional applications. *Adv. Mater.* **2024**, *36*, e2312263. DOI PubMed
37. Pan, S.; Liu, Z.; Wang, M.; et al. Mechanocombinatorially screening sensitivity of stretchable strain sensors. *Adv. Mater.* **2019**, *31*, e1903130. DOI PubMed
38. Liu, Y.; Xu, Z.; Ji, X.; et al. Ag-thiolate interactions to enable an ultrasensitive and stretchable MXene strain sensor with high temporospatial resolution. *Nat. Commun.* **2024**, *15*, 5354. DOI PubMed PMC
39. Dai, L.; Wang, L.; Chen, B.; Xu, Z.; Wang, Z.; Xiao, R. Shape memory behaviors of 3D printed liquid crystal elastomers. *Soft. Sci.* **2023**, *3*, 5. DOI
40. Kang, M.; Jeong, H.; Park, S. W.; et al. Wireless graphene-based thermal patch for obtaining temperature distribution and performing thermography. *Sci. Adv.* **2022**, *8*, eabm6693. DOI PubMed PMC
41. Chao, M.; Di, P.; Yuan, Y.; Xu, Y.; Zhang, L.; Wan, P. Flexible breathable photothermal-therapy epidermic sensor with MXene for ultrasensitive wearable human-machine interaction. *Nano. Energy.* **2023**, *108*, 108201. DOI
42. Park, Y.; Kwon, K.; Kwak, S. S.; et al. Wireless, skin-interfaced sensors for compression therapy. *Sci. Adv.* **2020**, *6*, eabe1655. DOI PubMed PMC
43. Chi, D.; Gu, H.; Wang, J.; et al. Narrow response temperature range with excellent reversible shape memory effect for semi-crystalline networks as soft actuators. *Mater. Horiz.* **2023**, *10*, 2464-75. DOI PubMed

Disclaimer/Publisher's Note: All statements, opinions, and data contained in this publication are solely those of the individual author(s) and contributor(s) and do not necessarily reflect those of OAE and/or the editor(s). OAE and/or the editor(s) disclaim any responsibility for harm to persons or property resulting from the use of any ideas, methods, instructions, or products mentioned in the content.



© The Author(s) 2026. Open Access This article is licensed under a Creative Commons Attribution 4.0 International License (https://creativecommons.org/licenses/by/4.0/), which permits unrestricted use, sharing, adaptation, distribution and reproduction in any medium or format, for any purpose, even commercially, as long as you give appropriate credit to the original author(s) and the source, provide a link to the Creative Commons license, and indicate if changes were made.